Petroleum Science 23 (2026) 928–938

Contents lists available at ScienceDirect

Petroleum Science

journal homepage: www.keaipublishing.com/en/journals/petroleum-science

Original Paper

Competition between viscous and capillary forces triggers diversity of fluid distribution and imbibition modes

Jin-Xin Cao [a,b], Yi-Qiang Li [a,b], Yu-Ling Zhang [c], Ya-Qian Zhang [a,b], Zhe-Yu Liu [a,b,*], Qi-Hang Li [a,b], Xue-Chen Tang [d], Tao Song [a,b]

[a] State Key Laboratory of Petroleum Resources and Engineering, China University of Petroleum (Beijing), Beijing, 102249, China
[b] College of Petroleum Engineering, China University of Petroleum (Beijing), Beijing, 102249, China
[c] No. 10 Oil Production Plant of PetroChina Changqing Oilfield Company, Qingyang, 745799, Gansu, China
[d] Exploration and Development Research Institute of PetroChina Southwest Oil & Gas Field Company, Chengdu, 610041, Sichuan, China

ARTICLE INFO

Article history:
Received 3 May 2025
Received in revised form
30 September 2025
Accepted 30 September 2025
Available online 6 October 2025

Edited by Yan-Hua Sun

Keywords:
Microfluidics
Imbibition mode
Instability
Remaining oil
Porous media

ABSTRACT

Spontaneous imbibition is the process in which the wetting phase displaces a non-wetting phase under the action of capillary forces. However, variations in interfacial properties, imbibition directions, and fractures result in different imbibition modes, posing challenges to a comprehensive understanding of the process. In this study, microfluidic chips representing matrix and fracture–matrix systems were designed. Imbibition agents with varied interfacial properties were selected to conduct experiments under counter-current and co-current conditions. A flow factor (γ), related to fracture geometry and imbibition direction, was defined and used together with the microscopic capillary number (Ca_{micro}) to characterize the imbibition process. Three distinct imbibition modes were observed for different Ca_{micro} and γ, clearly separated by γ–Ca_{micro} boundaries. During co-current imbibition, an unusual capillary-driven displacement process was observed, leading to fingering in the fracture–matrix model and leaving a large area of macroscale remaining oil. Smaller Ca_{micro} and fracture development will facilitate this process. In addition, various forms of microscale remaining oil, caused by bypass flow snap-off and Saffman–Taylor instability/Rayleigh–Taylor instability, were also observed across different imbibition processes. This study elucidates the imbibition mechanisms under the combined influence of capillary and viscous forces, providing deeper insights into the imbibition process in porous media.

1. Introduction

Two-phase flow in porous media is common in natural processes such as oil recovery (Aliabadian et al., 2022; Taman et al., 2025), carbon dioxide sequestration (Singh et al., 2023; Yu et al., 2025), and groundwater seepage (Wang et al., 2024; Yang et al., 2022). A typical case is the spontaneous imbibition, where the wetting phase replaces the non-wetting phase under the combined action of capillary and viscous forces (Malenica et al., 2024; Zhang et al., 2025). The imbibition process, affected by two-phase interface properties, imbibition direction, and fracture, exhibits complex flow modes. These modes significantly influence the distribution of remaining oil, often resulting in low recovery factor (Cai et al., 2022; Shoukry et al., 2023; Yadali Jamaloei et al., 2010). Understanding the controlling factors and formation mechanisms of imbibition is essential for interpreting pore-scale two-phase flow and enhance oil recovery (Ghodsi and Rasaei, 2025; Seetharaman et al., 2025; Zhang and Wang, 2022).

Research on pore-scale imbibition mainly involves numerical simulations and experiments (Cheng et al., 2023; Niu et al., 2022; Yu et al., 2021; Zhong et al., 2025). However, the accuracy of numerical simulations is often questioned, particularly when surfactants are involved, as they alter oil–water interfacial properties and increase model complexity (Chen et al., 2023). With the advancement of imaging and monitoring techniques, many experimental studies have been conducted on the pore-scale imbibition process (Li et al., 2014; Park et al., 2025). Du et al. (2024) developed an online physical simulation method

* Corresponding author.
E-mail address: zheyu.liu@cup.edu.cn (Z.-Y. Liu).
Peer review under the responsibility of China University of Petroleum (Beijing).

https://doi.org/10.1016/j.petsci.2025.09.043

combining nuclear magnetic resonance (NMR) and fractal theory, dividing displacement–imbibition coupling into three production stages. Lu et al. (2022) analyzed the effects of mineral content and fractures on coal imbibition using in situ dynamic micro-CT imaging, identifying four distinct stages. Liu et al. (2024) investigated microscopic imbibition and formation plugging mechanisms in tight reservoirs based on scanning electron microscopy (SEM) and nuclear magnetic resonance (NMR). These studies reveal a contradiction between resolution and field of view. Moreover, most methods rely on inversion techniques, which are costly and offer limited visual clarity.

Microfluidic technology has been increasingly applied in the oil industry due to its real-time monitoring, repeatability, and low cost (Gang et al., 2025; Jamieson et al., 2019). Tliba et al. (2025) combined core experiments and microfluidic to show how nanofluids enhance recovery by reducing interfacial tension (IFT), altering wettability, and forming stable oil-in-water emulsions. Lv et al. (2025) established a micro-nano scale natural pore structure chip and found that enhanced imbibition promotes fracturing fluid diffusion into matrix pores, increasing imbibition efficiency by 3%–6%. Mahmoudzadeh et al. (2022) highlighted the role of microemulsion formation and elastic oil–water interfaces in spontaneous imbibition within fractured porous media. Charpentier et al. (2018) highlighted the significance of Laplace pressure and viscosity in fluid fracture behavior within asymmetric Y-junctions. However, most studies use models of very limited scale, restricting investigations of large-scale sweep efficiency, imbibition modes, and remaining oil patterns. Large-scale microfluidic experiments are thus needed to link pore-scale mechanisms with macroscale flow behavior.

The balance among capillary force, viscous force, interfacial tension, and gravity determines the flow characteristics of pore-scale imbibition, resulting in phenomena such as stable imbibition, capillary fingering, and viscous fingering (Cardona and Santamarina, 2023; Chen et al., 2023; Hu et al., 2018; Lenormand et al., 1988). Cardona and Santamarina (2023) defined different imbibition modes based on the dimensionless ratio between advection-dominant flow and capillary-driven matrix imbibition in fractures using fluorescence microscopy and microfluidics. Sun et al. (2022) used a T-shaped microfluidic model to study the interplay among fluid velocity, interfacial tension, and viscosity, analyzing the tensile and fracture behavior of crude oil transitioning from throat to pore in the presence of active nanofluids. Lei et al. (2023) revealed that strong depth confinement inhibits unstable interfacial behavior and incomplete imbibition modes by analyzing capillary numbers and depth variation factors. Odier et al. (2017) combined high-resolution imaging and confocal microscopy to demonstrate that two liquid-entrainment transitions and Rayleigh–Plateau instabilities govern four pore-scale imbibition scenarios. Holtzman and Segre (2015) studied the effect of wettability on the immiscible displacement of viscous fluids in disordered porous media, showing that increasing the wettability of the invading fluid promotes cooperative pore filling and stabilizes invasion, further deriving two dimensionless numbers to predict displacement modes. The use of surfactants further complicates interfacial mechanics, affecting the balance of driving and resisting forces and thus imbibition efficiency (Suetrong et al., 2024; Sukee et al., 2022a; Tangparitkul et al., 2023). Tangparitkul et al. (2024) demonstrated a distinct difference between surfactants and nanofluids in capillary-driven oil recovery, challenging the assumption that nanofluid-induced interfacial tension reduction is the primary mechanism for EOR. Akamine et al. (2024) found that the interfacial properties of nanofluids at different concentrations vary significantly, leading to different mechanisms of remaining oil formation at different pore scales and thus affecting the final imbibition efficiency. Sukee et al. (2022a) believed that a water-wet system requires a larger interfacial tension to increase the imbibition driving force, while an oil-wet system requires a smaller interfacial tension to reduce the imbibition resistance. Nevertheless, experimental studies focusing on the role of surfactants under different imbibition conditions remain limited, and the integrated analysis of macroscale imbibition modes and pore-scale mechanisms is still lacking.

To address these issues, this study designed microfluidic chips simulating both matrix and fracture–matrix systems. The effects of two-phase interface properties, fracture development degree, and imbibition direction were systematically investigated. Differences in imbibition modes under varying conditions were analyzed using microscopic capillary number (Ca_{micro}), and the formation mechanisms of remaining oil were explored through quantitative pore-scale analysis, providing new insights into the spontaneous imbibition process in porous media.

2. Materials and experimental method

2.1. Experimental fluids

The oil used in this study is crude oil from oilfield, with a viscosity of 13.7 mPa·s and a density of 0.817 g/cm^3 at 25 °C. The synthetic water has a total dissolved solids (TDS) concentration of 112,767 mg/L, and its ionic composition is listed in Table 1. The experimental agents include analytically pure sodium α-olefin sulfonate (AOS, $C_3H_5SO_3Na$, from Merck KGaA, China), sodium fatty alcohol ether sulfate (AES, $C_{12}H_{25}(OC_2H_4)_2OSO_3Na$, from Chron Chemicals, China), sodium dodecyl sulfate (SDS, $C_{12}H_{25}OSO_3Na$, from Aladdin, China), and *n*-butanol (C_4H_9OH, from Macklin, China).

To analyze the influence of interfacial properties on the imbibition effect, five agents were prepared. (1) Simulated formation water (SFW) served as the control group. (2) AES, AOS, and SDS solutions were surfactant solutions with mass fraction of 0.5% in SFW. (3) Microemulsion system was a surfactant solution that can form in-situ microemulsion, composed of 5% AOS and 8% *n*-butanol.

2.2. Microfluidic experimental setup

The experimental setup consists of two main components: the experimental and acquisition modules (Fig. 1(a)). The experimental module includes a Harvard PhD ultra-symphony pump, a SEENO LED surface light source for illumination, a beaker for waste collection, and a microscopic glass model. The acquisition module includes a Sony A7M4 camera with an FE 90 mm f/2.8 macro lens for image recording and a computer for image storage and analysis. Two types of microfluidic chips were used in this experiment: matrix and fracture–matrix. Taking the matrix chip as an example, the model measures 97 mm in length and 37 mm in width. The chip structure is formed by repeating a basic unit, with a minimum pore radius of 22.35 μm, a maximum pore radius of 911 μm, and an average pore radius of 240 μm. Please refer to Table 2 for detailed model parameters. It is worth noting that the model used in this study has an overall size of 97,000 μm × 37,000 μm. During imaging, the pixel resolution is 7509 × 2856 in the horizontal and vertical directions, respectively, resulting in a pixel size of 12.9365

Table 1
Ionic composition of synthetic water.

Ion	$K^+ + Na^+$	Ca^{2+}	Mg^{2+}	Cl^-	SO_4^{2-}	HCO_3^-
Concentration, mg/L	41612	1619	432	65710	2545	849

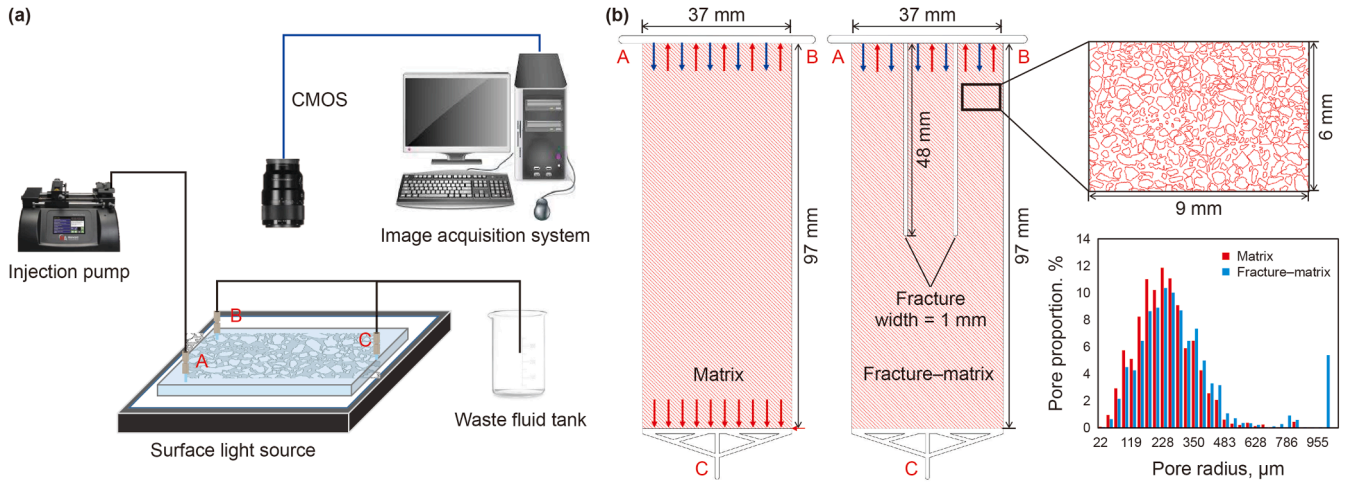

Fig. 1. The schematic diagram of micromodel imbibition.

Table 2
Parameters of matrix and fracture–matrix models.

Model	Porosity, %	Length, mm	Width, mm	Average pore radius, μm
Matrix model	55	97	37	240
Fracture–matrix model	60	97	37	305

μm/pixel. This resolution corresponds to 1/37 of the average pore radius, which is sufficient for accurate image-based analysis.

A diversion channel is located at one end of the model to facilitate the circulation of the imbibition agent. The fracture–matrix chip contains two non-penetrating fractures based on the matrix chip. The pore radius distributions of both types of chips are shown in Fig. 1(b). Experiments under co-current and counter-current conditions were conducted. As shown in Fig. 1(b), during co-current imbibition, the agent is injected through port A and produced from ports B and C. Counter-current imbibition occurs when port C is closed. When the micromodel is undergoing co-current imbibition on the macroscopic scale, localized counter-current imbibition may occur simultaneously.

2.3. Experimental procedure and scheme

During the experiment, the microfluidic chip was first saturated with crude oil, and then the imbibition agent was continuously injected into the diversion channel at a rate of 2 μL/min. The experiment was conducted at 26 °C and standard atmospheric pressure and terminated when the oil–water distribution no longer changed. To record the imbibition process, images were captured every 30 s. In this study, two types of chips, matrix and fracture–matrix, were used to conduct experiments with five agents under both counter-current and co-current conditions. A total of 20 sets of experiments were conducted. All experiments were repeated twice. If the difference in recovery factor between the two experiments was less than 10%, the experimental results are considered valid. Otherwise, a third set of experiments will be added.

2.4. Image analysis

To gain deeper insights into the imbibition process, this study evaluated imbibition efficiency and pore-throat utilization characteristics. The relevant methods are described in our previous research (Cao et al., 2024, 2025; Gao et al., 2021).

2.5. Oil–water–rock interface property testing

2.5.1. Solubilization capacity

The oil–water solubilization capacity of the 5% AOS system was evaluated according to Southwick's oil–water phase behavior test method (Southwick et al., 2020). The procedure was as follows: 4 mL of surfactant solution was added to a test tube, followed by 4 mL of crude oil. After sealing, the test tube was shaken thoroughly and left to stand for two days, with shaking once daily. After two days, when oil and water reached equilibrium, the phase type and phase volume were recorded. The solubilization capacity was determined by calculating SP_X using the following equation (Huh, 1983).

$$SP_X = \frac{V_X}{V_S}$$

where SP_X is the amount of solubilized oil, dimensionless; V_X is the volume of oil entering the microemulsion, mL; V_S is the volume of surfactant, mL.

2.5.2. IFT

The interfacial tension (IFT) between crude oil and imbibition agents was measured using a TX-500C IFT meter (CNG Corporation, USA) at 5000 rpm. The IFT of the 5% AOS system was calculated using the Chun Huh equation based on the oil–water solubilization capacity SP_X of the middle-phase microemulsion (Spildo et al., 2014).

$$\sigma = \frac{C}{SP_X^2}$$

where σ is the IFT, mN/m; C is a constant, dimensionless, usually taken as 0.3.

2.5.3. Contact angle

The contact angle was measured using a Theta Flex optical tensiometer (Biolin Scientific, Sweden).

3. Result analysis

3.1. Interfacial properties of surfactants

The IFT between SFW and crude oil was 13.41 mN/m. The four surfactant systems reduced the IFT by over 85%, with AOS

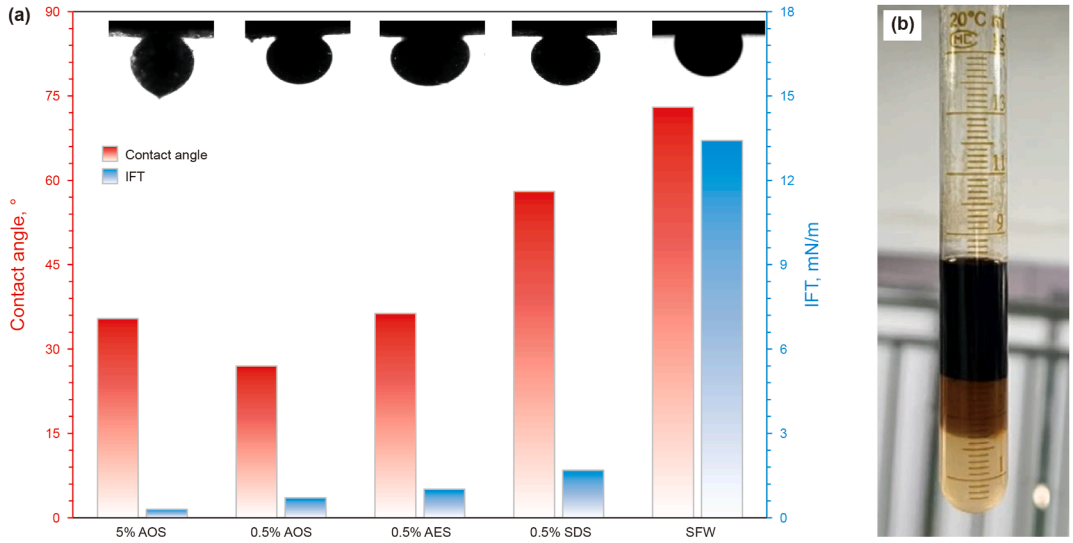

Fig. 2. Measurement results of properties of imbibition agents. (**a**) IFT and contact angle of different imbibition agents. (**b**) 5% AOS oil water solubilization capacity.

exhibiting the greatest reduction effect. When immersed in crude oil, the contact angle of the glass was 73°, indicating weak water-wet conditions. All four imbibition agents improved the wettability of the glass surface. The solubilization capacity SP_X of the 5% AOS system was 1, and the calculated IFT was 0.3 mN/m (Fig. 2).

3.2. Effect of different factors on imbibition efficiency

3.2.1. Oil–water interfacial properties

Fig. 3(a) presents the imbibition efficiency curves of different agents under counter-current imbibition in the matrix model. Among the five agents, 5% AOS exhibited the highest efficiency (0.54), while SFW showed the lowest (0.11). The efficiency ranking was: 5% AOS > 0.5% AOS > 0.5% AES > 0.5% SDS > SFW. The imbibition process consists of three main stages: capillary start-up, blocking equilibrium, and saturation equilibrium. During the capillary start-up stage, capillary forces drive the imbibition agent into small pore throats, displacing oil from larger pores and causing a rapid rise in efficiency. During the blocking equilibrium stage, capillary force weakens as the agent advances, while the complex oil–water distribution increases flow resistance. These forces reach a near balance, resulting in a slow efficiency increase over an extended period. Agents with lower IFT and greater wettability enhancement achieve higher imbibition efficiency at this stage. At the saturation equilibrium stage, pores near the diversion channel reach a remaining oil state, and driving forces balance resistance, causing imbibition efficiency to stabilize. However, the 5% AOS system, due to its solubilization capability, can further enhance efficiency by forming microemulsions. The results also showed that higher IFT shortened the time to reach stable imbibition efficiency.

Fig. 3(b) plots the final efficiency of pores with different sizes. Unlike displacement processes, which tend to sweep macropores, the imbibition process uniformly sweeps pores of all sizes. The observed fluctuation in macropores and fractures results from the sparse development of such structures in the matrix model. Compared with the 0.5% AOS system, the 5% AOS system significantly improved the imbibition efficiency of mesopores, contributing to its higher overall efficiency.

In pore-scale two-phase flow, the definition of the capillary number (Ca), describing the balance between viscous and capillary forces and predicting non-wetting phase mobilization, was employed. Ca only considers the influence of interfacial tension, in fact, capillary force is the main factor determining imbibition, therefore both the microscopic capillary number (Ca_{micro}) and the macroscopic capillary number (Ca_{macro}) were employed in this study (Armstrong et al., 2014; Hilfer et al., 2015; Lei et al., 2023).

$$Ca_{micro} = \frac{\eta_{agent} v}{\sigma}$$

$$Ca_{macro} = \frac{\eta_{agent} \phi v L}{k P_c}$$

$$P_c = \frac{2\sigma\cos(\theta)}{R}$$

where η_{agent} is the viscosity of imbibition agent, $\eta_{agent} = 1$ mPa·s; v is the characteristic velocity of the crude oil phase, $v = 1 \times 10^{-6}$ m/s (Sukee et al., 2022b); σ is the oil–agent IFT, N/m; ϕ, L, k, and R are the matrix porosity (dimensionless), length (m), permeability (m^2), and average pore size of the designed microfluidic model (m); and θ is the contact angle between the oil, agent, and pore surface, °. The permeability of the micromodel was calculated by the Kozeny–Carman equation (Wu et al., 2023).

The results showed a strong positive correlation between Ca_{micro}/Ca_{macro} and imbibition efficiency, following a logarithmic relationship (Fig. 3(c)). By arranging the images captured at the end of imbibition according to increasing Ca_{micro}/Ca_{macro}, a series of images with increasing imbibition distances and efficiencies were obtained (Fig. 3(d)). This indicates that during counter-current imbibition, a higher Ca_{micro} generally corresponds to a longer imbibition distance and higher efficiency.

3.2.2. Imbibition direction

During co-current imbibition, the efficiency was significantly higher than that of counter-current imbibition, with an average increase of 41% (Fig. 4(a)). In the co-current imbibition process, the efficiency gradually increases logarithmically with rising Ca_{micro}/Ca_{macro} (Fig. 4(b)). Those process also consists of three stages. The time required to reach half of the final efficiency indicates that, although co-current imbibition achieves higher efficiency, it takes longer to complete, and the process time increases as Ca_{micro}

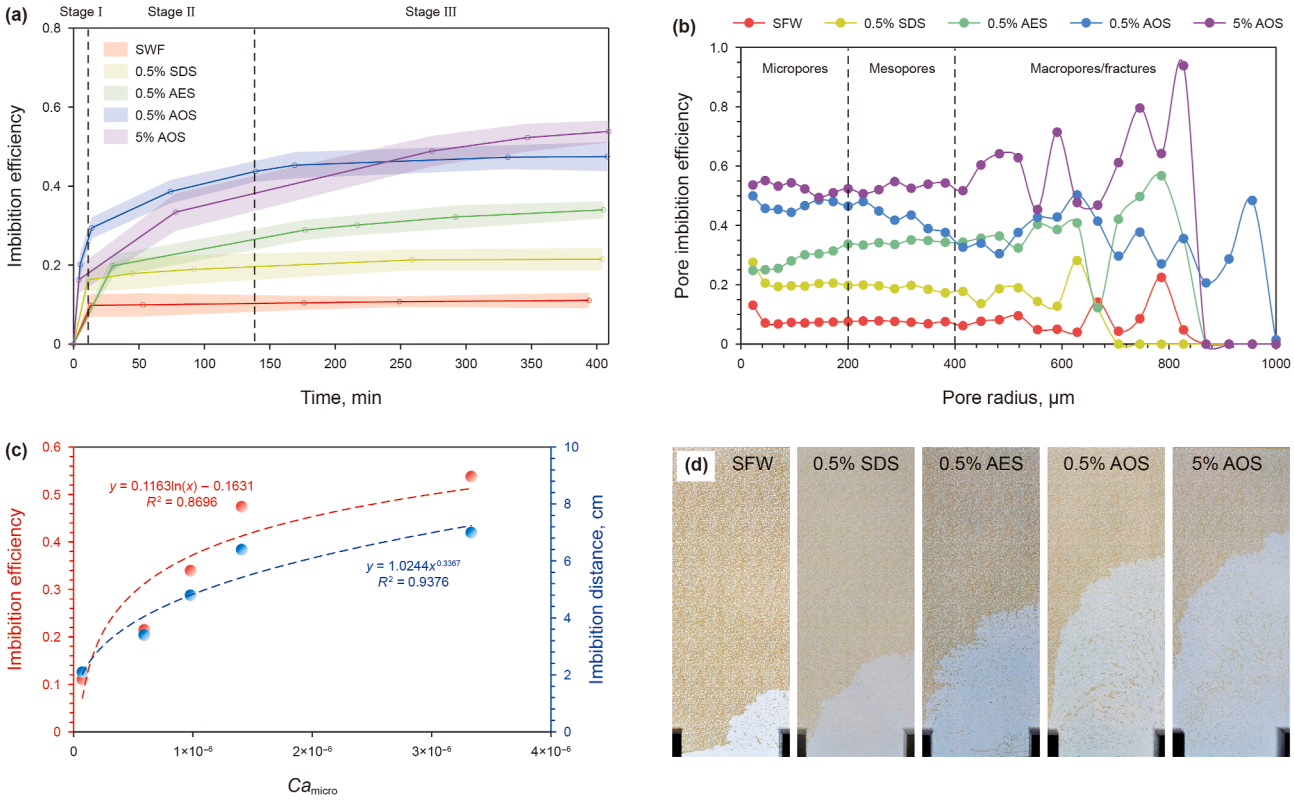

Fig. 3. Counter-current imbibition efficiency of different agents. (**a**) Imbibition efficiency curves of different agents. (**b**) Pore-scale imbibition efficiency curves of different agents. (**c**) Relationship between imbibition efficiency, distance and Ca_{micro}. (**d**) Remaining oil distribution after counter-current imbibition.

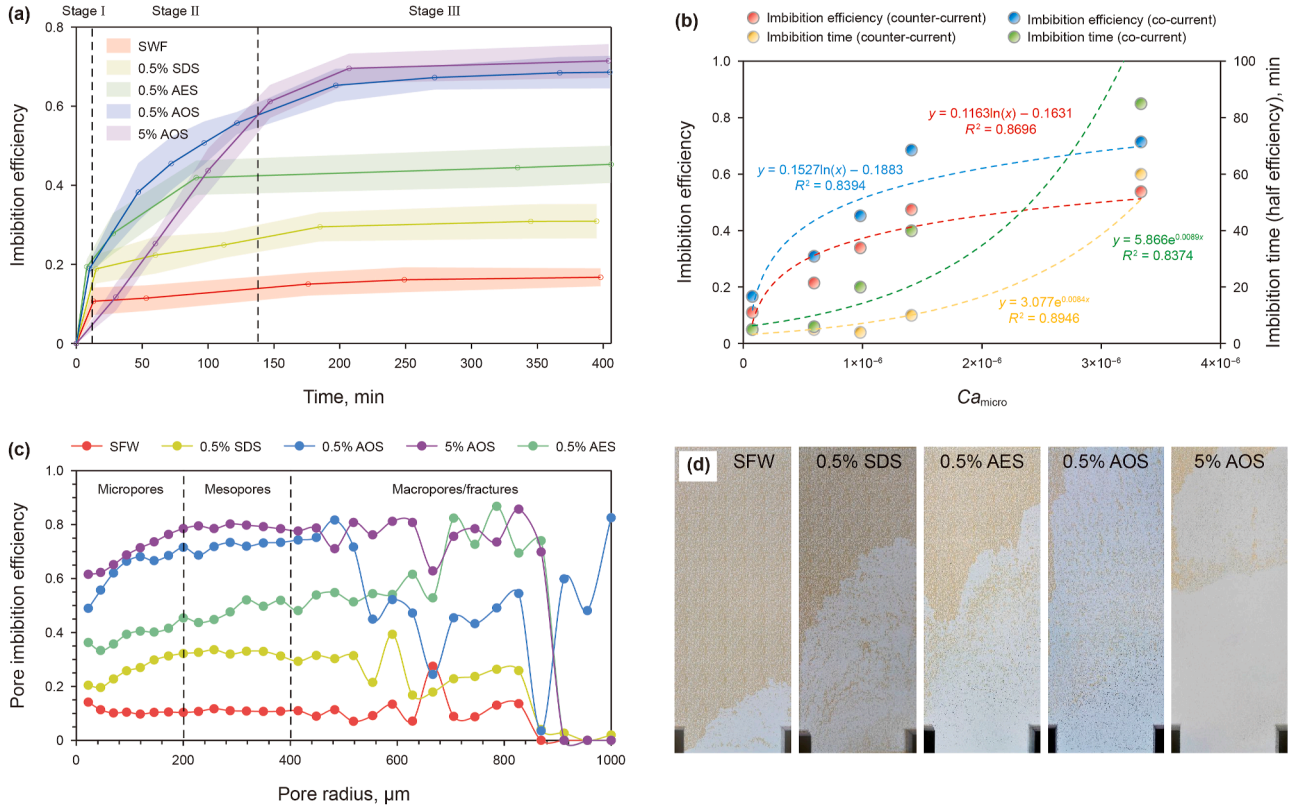

Fig. 4. Co-current imbibition efficiency of different agents. (**a**) Imbibition efficiency curves of different agents. (**b**) Relationship between imbibition efficiency, time and Ca_{micro}. (**c**) Pore-scale imbibition efficiency curves of different agents. (**d**) Remaining oil distribution after co-current imbibition.

increases (Fig. 4(b)). Pore throat mobilization in co-current imbibition differs from that in counter-current imbibition. The results indicate that co-current imbibition exhibits displacement-like characteristics, with reduced small-pore mobilization and enhanced large-pore mobilization (Fig. 4(c) and (d)).

To analyze this feature, a model was established as shown in Fig. 5(a), where 0–6 represent throats of different sizes. In this process, the agent initially flows along the diversion channel. In the water wet model, under the influence of capillary forces, the agent first enters the smaller throat (throat 1) and reaches throat 2 (Fig. 5(b)). During counter-current imbibition, the agent cannot reach deeper throats (throats 3–6) and can only exit through throat 0, as indicated by the yellow arrow in Fig. 5(c). During co-current imbibition, the agent can overcome the viscous force generated by crude oil flow driven by capillary force to enter larger throat with less resistance (throat 3), as indicated by the green arrow in Fig. 5 (d). This displacement effect under capillary force results in higher efficiency in co-current imbibition and makes the pore throat mobilization resemble that in displacement processes.

3.2.3. Fracture development degree

Fig. 6(a) shows the imbibition efficiency curves of the 5% AOS and SFW systems during the counter-current imbibition process in the matrix and fracture–matrix models. Fracture significantly enhances imbibition efficiency and expands the sweep area, as shown in Fig. 6(b). Compared to the matrix model, imbibition efficiency increases by 0.21 and 0.14, respectively. The histogram of pore throat imbibition efficiency in different models of the 5% AOS system shows that oil in fractures undergoes comprehensive sweep during imbibition (Fig. 6(c) and (d)). Additionally, the increased contact area between fractures and matrix pores significantly improves imbibition efficiency in matrix pores due to the expanded sweep area.

3.3. Transformation from complete to incomplete imbibition based on microscopic capillary number

This study defines the flow factor γ to analyze the characteristics of the imbibition process. Specifically, the γ values for the counter-current and co-current imbibition in the matrix model are 1 and 2, respectively, while in the fracture–matrix model, they are 3 and 4 (Table 3). It is evident that as γ increases, the boundary conditions become more favorable for imbibition. A γ–Ca_{micro} (Ca_{macro}) intersection diagram was plotted to illustrate the regularity of the imbibition process. The results indicated that, under low γ and Ca_{micro}, incomplete imbibition with limited swept distance occurred, whereas under high γ and Ca_{micro}, complete imbibition covered the entire model. As Ca_{micro} and γ increased, the imbibition distance gradually expanded (Fig. 7). A dividing line was observed that separated incomplete imbibition from complete imbibition.

A transition zone between incomplete and complete imbibition was identified (Fig. 8(a)). To quantitatively analyze the impact of agent type and conditions on the imbibition mode, 2D semi-log plot showing the imbibition distance under different Ca_{micro} and γ was plotted by scattered data interpolation methods (Amidror, 2002). Three distinct imbibition modes—complete, transition, and incomplete—were identified by taking the full model (9.70 cm) and half model (4.85 cm) imbibition distances as the boundaries (Fig. 8

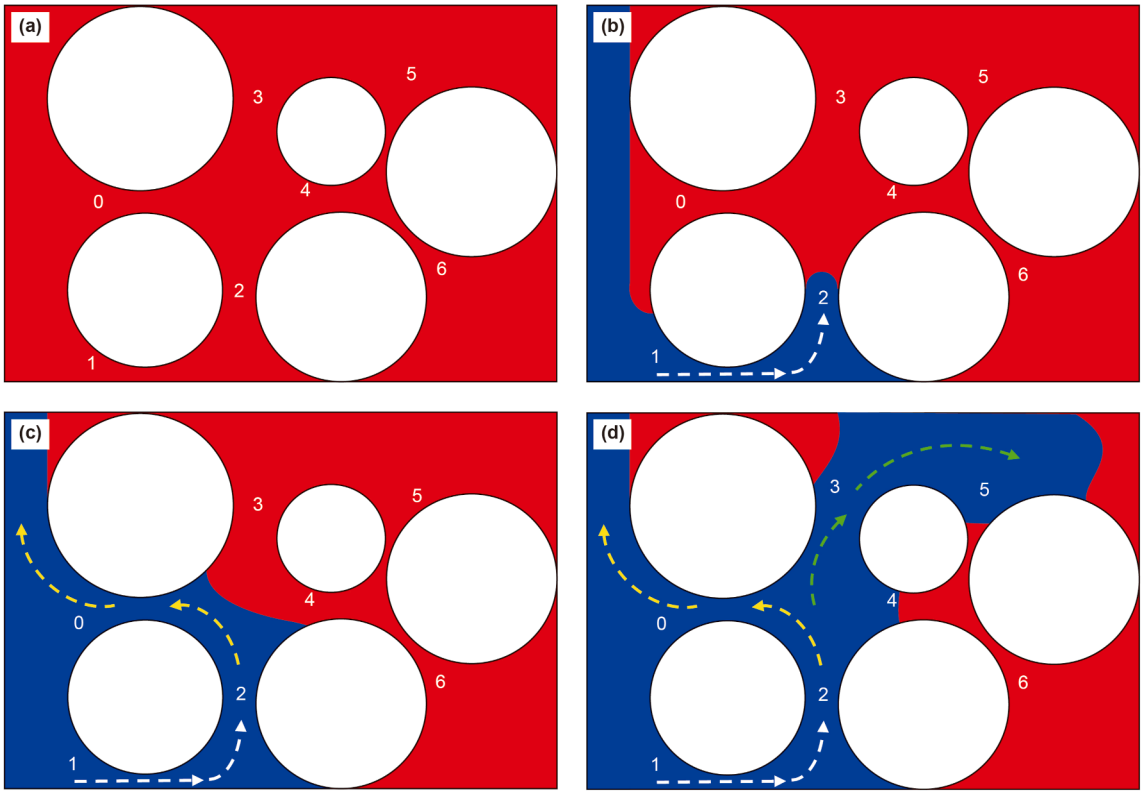

Fig. 5. Capillary force displacement in co-current imbibition process.

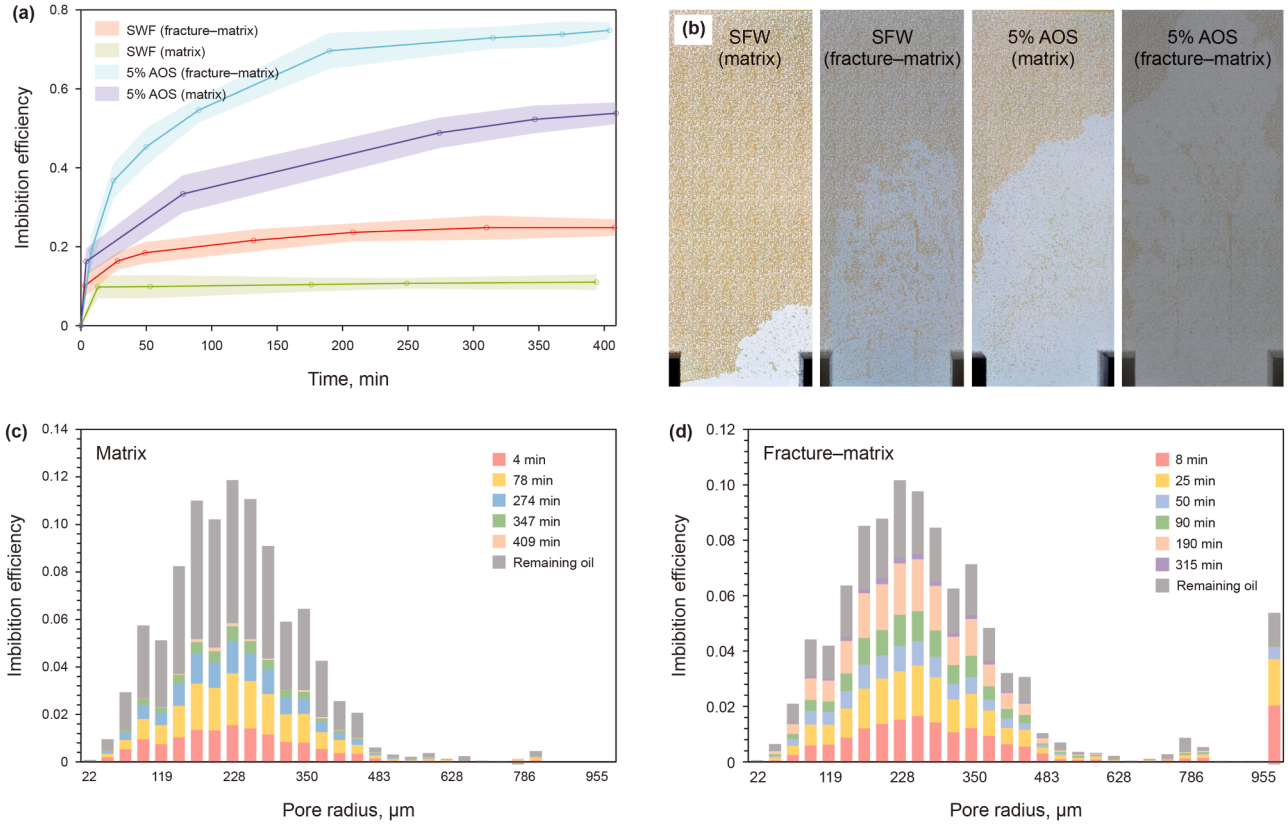

Fig. 6. Imbibition efficiency of matrix and fracture–matrix model. (**a**) Imbibition efficiency curves. (**b**) Oil water distribution at the end moment. (**c**) Pore throat imbibition efficiency of 5% AOS system in the matrix model. (**d**) Pore throat imbibition efficiency of 5% AOS system in the fracture–matrix model.

Table 3
Setting of experimental conditions for microfluidic.

Flow factor γ	Imbibition direction	Fracture development degree
1	Counter-current	Matrix
2	Co-current	Matrix
3	Counter-current	Fracture–matrix
4	Co-current	Fracture–matrix

(b)). Both increasing Ca_{micro} and modifying imbibition conditions significantly influenced mode transition. However, modifying conditions was more effective in expanding the swept area.

3.4. Instability of imbibition process caused by viscous and capillary forces

The instability in the oil–water displacement process results in significant remaining oil, which can be categorized into two main types: microscale and macroscale remaining oil.

3.4.1. Macroscale remaining oil

Macroscale remaining oil refers to the remaining oil distributed throughout the entire model. This type of remaining oil results from the displacement effect of capillary forces on crude oil and commonly occurs during co-current imbibition (Fig. 10). During co-current imbibition, the imbibing agent displaces along the blue dotted lines. In Fig. 9(a) and (c), displacement effect of capillary force can significantly improve the sweep efficiency along the blue dotted lines. In Fig. 9(b) and (d), the displacement by capillary forces causes viscous fingering due to Saffman–Taylor instability (Tangparitkul et al., 2024), significantly reducing the sweep efficiency. At this stage, the imbibing agent flows along the yellow and green dotted lines, gradually moving toward the inlet and outlet driven by capillary forces. AES, SDS, and SFW with smaller Ca_{micro} are more likely to exhibit this behavior. That is, stronger capillary forces or weaker viscous forces intensify instability caused by capillary displacement. The development of fractures increases model heterogeneity, intensifying this instability and broadening the macroscale distribution of remaining oil. This suggests that fractures may decrease imbibition efficiency under specific conditions.

3.4.2. Microscale remaining oil

Microscale remaining oil can be classified into three main types based on their formation mechanisms. The first type is cluster-like remaining oil, shown in Fig. 10(a), formed by the Jamin effect caused by pore structure heterogeneity and bypass flow (Li et al., 2025) (Fig. 10(b) and (c)). The second type is droplet-like remaining oil with a regular shape, shown in Fig. 10(d). This type remaining oil forms when the wetting phase displaces the non-wetting phase, causing the latter to break up due to strong wall flow through pore throats of varying diameter (Lei et al., 2023). Under the Jamin effect, oil droplets cannot pass through smaller throats, leading to remaining oil formation. This type of residual oil is often found in pore throats with large radius differences, such as fractures (Fig. 10(e)–(h)). This snap-off process may be similar to the Haines jump. The final type is film-like remaining oil, shown in Fig. 10(i). Due to the high density and low viscosity of the imbibition agent, it passes through the pore centers during the capillary displacement process, leaving a large amount of oil on the pore surfaces due to Saffman–Taylor (Saffman and Taylor, 1988; Zhang et al., 2023) and Rayleigh–Taylor (Cabot and Cook, 2006;

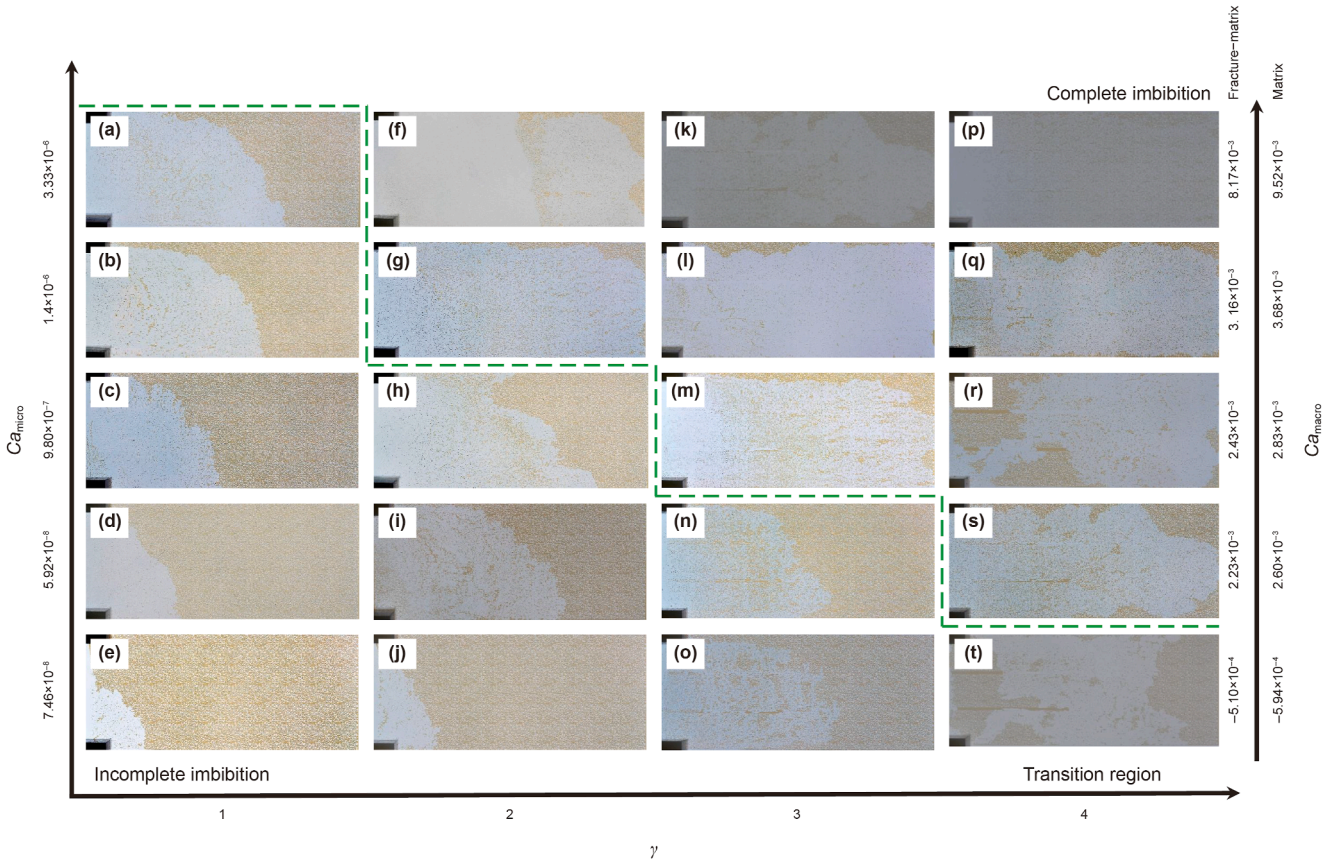

Fig. 7. γ–Ca_{micro} (Ca_{macro}) intersection diagram of different imbibition conditions.

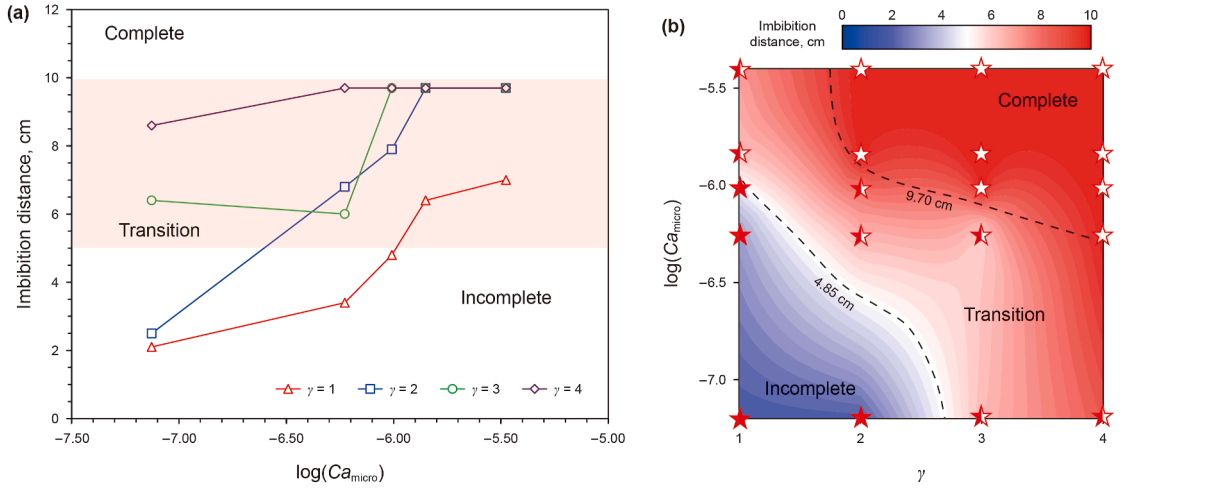

Fig. 8. Imbibition modes under different conditions. (**a**) Imbibition distance under different Ca_{micro} and γ. (**b**) 2D semi-log plot showing the imbibition distance under different Ca_{micro} and γ.

Kuranz et al., 2018) instabilities (Fig. 10(j) and (k)). This phenomenon was observed only in the 5% AOS agent under co-current imbibition. The combined effect of capillary and viscous forces leads to the formation of the three types of microscale remaining oil, controlling the complex oil–water distribution during the imbibition process.

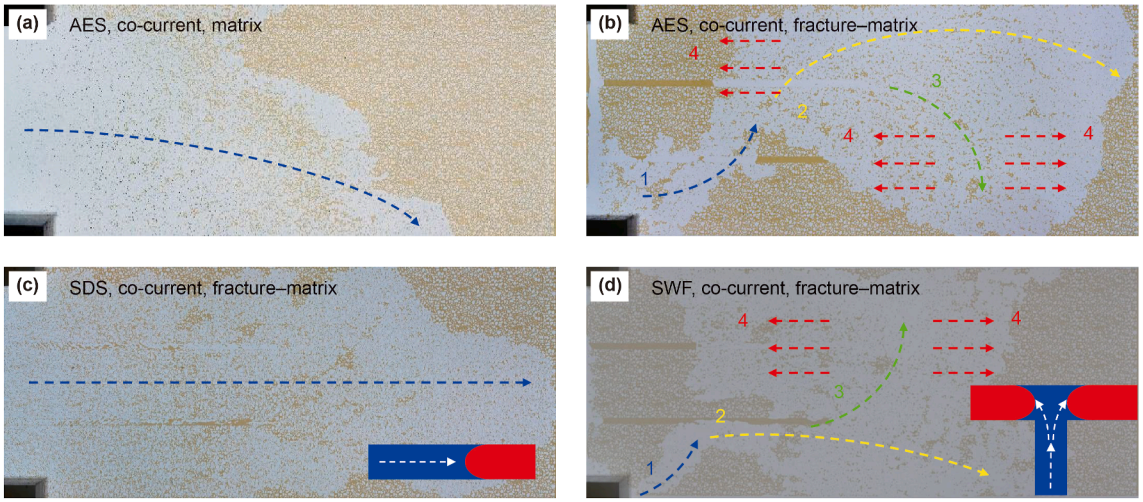

Fig. 9. Macroscale remaining oil distribution characteristics under capillary force displacement.

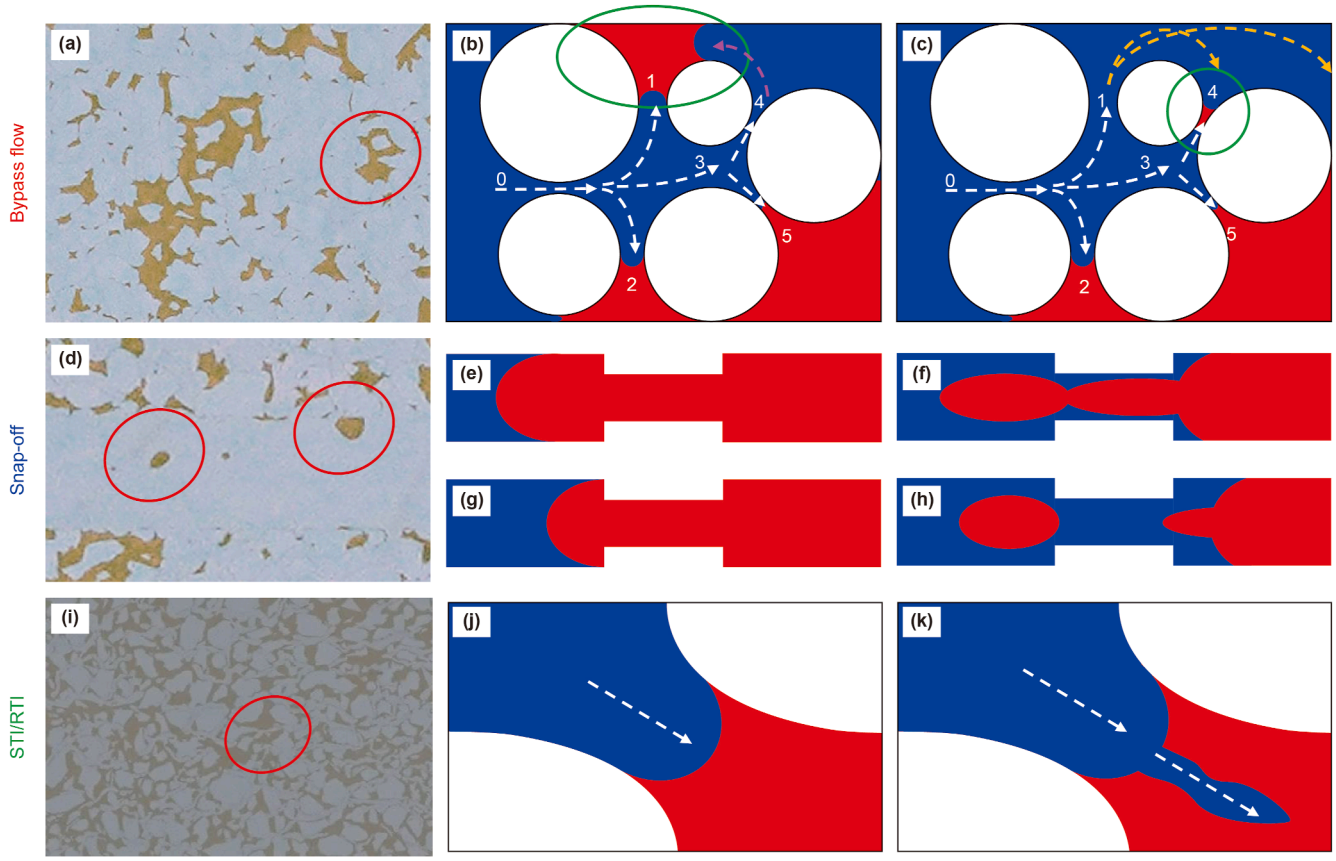

Fig. 10. Three types of microscale remaining oil during imbibition. (**a**)–(**c**) Cluster-like remaining oil caused by bypass flow. (**d**)–(**h**) Droplet-like remaining oil caused by snap-off. (**i**)–(**k**) Film-like remaining oil caused by Saffman–Taylor instability (STI) and Rayleigh–Taylor instability (RTI).

4. Conclusions

This study focuses on the imbibition process in microfluidic, analyzing the effects of two-phase interface properties, imbibition direction, and fractures. Three imbibition modes and the origins of remaining oil were also discussed. The main conclusions are as follows.

(1) As Ca_{micro} increases, the imbibition efficiency and distance increase logarithmically. Counter-current imbibition exhibits a uniform pore mobilization pattern, characterized by small pore suction and large pore discharge. During co-current imbibition, an unusual capillary force displacement phenomenon was observed, causing fingering along macropores, which is similar to displacement processes.

Regardless of conditions, imbibition processes include three stages: capillary start-up, blocking equilibrium, and saturation equilibrium.

(2) Incomplete imbibition with limited sweep distance occurs under conditions of low Ca_{micro} and γ. In contrast, high Ca_{micro} and γ conditions lead to complete imbibition with full sweep. A transition mode occurs between these two modes. Two distinct Ca_{micro}–γ boundaries separate these three modes.

(3) The remaining oil after imbibition can be categorized into microscale and macroscale types. The viscous fingering induced by capillary force displacement leads to the formation of macroscale remaining oil, which is particularly obvious in the co-current imbibition of fracture–matrix model. Microscopic remaining oil is divided into three types: cluster-like residual oil caused by bypass flow and pore throat heterogeneity, droplet-like remaining oil caused by snap-off due to pore throat radius differences, and film-like remaining oil caused by Saffman–Taylor and Rayleigh–Taylor instabilities arising from fluid property differences.

Although this study provides a detailed analysis, several issues remain unresolved. These include finding a quantitative parameter to replace the flow factor, and determining the parameters that controlled the critical formation conditions for the microscale remaining oil.

CRediT authorship contribution statement

Jin-Xin Cao: Writing – original draft, Visualization, Software, Methodology, Conceptualization. **Yi-Qiang Li:** Supervision, Funding acquisition. **Yu-Ling Zhang:** Writing – review & editing, Investigation, Data curation. **Ya-Qian Zhang:** Writing – original draft, Validation, Software. **Zhe-Yu Liu:** Validation, Supervision, Conceptualization. **Qi-Hang Li:** Visualization, Investigation. **Xue-Chen Tang:** Writing – original draft, Visualization, Validation. **Tao Song:** Writing – review & editing, Investigation, Conceptualization.

Declaration of competing interest

The authors declare that they have no known competing financial interests or personal relationships that could have appeared to influence the work reported in this paper.

Acknowledgment

The authors thank the National Natural Science Foundation of China (Grant No. U23B6003) and the National Major Science and Technology Project of China (Grant No. 2025ZD1406206) for the support of this work.

References

Akamine, T., Tosuai, T., Ramadhan, R., Promsuk, N., Srisuriyachai, F., Tangparitkul, S., 2024. Visualizing oil displacement by nanofluids at pore scale: A concentration-dependent nanofluid spreading induced by structural disjoining pressure. Capillarity 12 (1), 17–26. https://doi.org/10.46690/capi.2024.07.03.

Aliabadian, E., Esmaeili, S., Sadeghi, S., Maini, B., Sundararaj, U., Chen, Z., 2022. New insight to polymer transport in porous media to enhance heavy oil recovery: Lab experiment and numerical simulation. Fuel 322, 124257. https://doi.org/10.1016/j.fuel.2022.124257.

Amidror, I., 2002. Scattered data interpolation methods for electronic imaging systems: A survey. J. Electron. Imag. 11 (2), 157–176. https://doi.org/10.1117/1.1455013.

Armstrong, R.T., Georgiadis, A., Ott, H., Klemin, D., Berg, S., 2014. Critical capillary number: Desaturation studied with fast X-ray computed microtomography. Geophys. Res. Lett. 41 (1), 55–60. https://doi.org/10.1002/2013GL058075.

Cabot, W.H., Cook, A.W., 2006. Reynolds number effects on Rayleigh–Taylor instability with possible implications for type Ia supernovae. Nat. Phys. 2 (8), 562–568. https://doi.org/10.1038/nphys361.

Cai, J., Chen, Y., Liu, Y., Li, S., Sun, C., 2022. Capillary imbibition and flow of wetting liquid in irregular capillaries: A 100-year review. Adv. Colloid Interface Sci. 304, 102654. https://doi.org/10.1016/j.cis.2022.102654.

Cao, J., Li, Y., Zhang, Y., Gao, W., Zhang, Y., Cai, Y., Tang, X., Li, Q., Liu, Z., 2024. Identification of polymer flooding flow channels and characterization of oil recovery factor based on U-net. In: SPE Conf. Oman Petrol. Energy Show. https://doi.org/10.2118/218767-MS.

Cao, J., Li, Y., Zhang, Y., Tang, X., Liu, Z., Li, Q., Song, T., Zhang, Y., 2025. Viscous and capillary forces competition triggered flow instability in porous media. Phys. Fluids 37, 082138. https://doi.org/10.1063/5.0281257.

Cardona, A., Santamarina, J.C., 2023. Immiscible imbibition in fractured media: A dual-porosity microfluidics study. Int. J. Rock Mech. Min. Sci. 170, 105555. https://doi.org/10.1016/j.ijrmms.2023.105555.

Charpentier, J.B., Bizet, L., Saouab, A., 2018. Gravity induced fluid fragmentation in an asymmetric microfluidic Y junction. J. Colloid Interface Sci. 532, 300–308. https://doi.org/10.1016/j.jcis.2018.07.117.

Chen, X., Li, Y., Liu, Z., Trivedi, J., Tang, Y., Sui, M., 2023. Visualized investigation of the immiscible displacement: Influencing factors, improved method, and EOR effect. Fuel 331, 125841. https://doi.org/10.1016/j.fuel.2022.125841.

Cheng, Z., Gao, H., Tong, S., Zhang, W., Ning, Z., 2023. Pore scale insights into the role of inertial effect during the two-phase forced imbibition. Chem. Eng. Sci. 278, 118921. https://doi.org/10.1016/j.ces.2023.118921.

Du, M., Zhengming, Y., Lv, W., Xiao, Q., Xiang, Q., Yao, L., Feng, C., 2024. Experimental study on microscopic production characteristics and influencing factors during dynamic imbibition of shale reservoir with online NMR and fractal theory. Energy 310, 133244. https://doi.org/10.1016/j.energy.2024.133244.

Gang, H., Yang, M., Chen, Q., Su, Z., Sun, G., Wang, W., Yang, S., Li, Y., Mu, B., 2025. Oil displacement behavior of biosurfactant/chemically synthetic surfactant binary system in a microfluidic chip. Geoenergy Sci. Eng. 251, 213902. https://doi.org/10.1016/j.geoen.2025.213902.

Gao, W., Li, Y., Zhang, J., Luan, H., Cao, H., Yu, Z., 2021. Effect of surfactant on pore-scale mobilization characteristics in various pore structure conglomerate for enhanced oil recovery. Colloids Surf. A Physicochem. Eng. Asp. 627, 127150. https://doi.org/10.1016/j.colsurfa.2021.127150.

Ghodsi, M., Rasaei, M.R., 2025. Uncovering the impact of morphology of porous media and capillary number on immiscible oil recovery using computational fluid dynamics. Geoenergy Sci. Eng. 244, 213408. https://doi.org/10.1016/j.geoen.2024.213408.

Hilfer, R., Armstrong, R.T., Berg, S., Georgiadis, A., Ott, H., 2015. Capillary saturation and desaturation. Phys. Rev. 92 (6), 063023. https://doi.org/10.1103/PhysRevE.92.063023.

Holtzman, R., Segre, E., 2015. Wettability stabilizes fluid invasion into porous media via nonlocal, cooperative pore filling. Phys. Rev. Lett. 115 (16), 164501. https://doi.org/10.1103/PhysRevLett.115.164501.

Hu, R., Wan, J., Yang, Z., Chen, Y.-F., Tokunaga, T., 2018. Wettability and flow rate impacts on immiscible displacement: A theoretical model. Geophys. Res. Lett. 45 (7), 3077–3086. https://doi.org/10.1002/2017GL076600.

Huh, C., 1983. Equilibrium of a microemulsion that coexists with oil or brine. SPE J. 23 (5), 829–847. https://doi.org/10.2118/10728-PA.

Jamieson, E.J., Fewkes, C.J., Berry, J.D., Dagastine, R.R., 2019. Forces between oil drops in polymer-surfactant systems: Linking direct force measurements to microfluidic observations. J. Colloid Interface Sci. 544, 130–143. https://doi.org/10.1016/j.jcis.2019.02.051.

Kuranz, C.C., Park, H.S., Huntington, C.M., Miles, A.R., Remington, B.A., Plewa, T., Trantham, M.R., Robey, H.F., Shvarts, D., Shimony, A., Raman, K., MacLaren, S., Wan, W.C., Doss, F.W., Kline, J., Flippo, K.A., Malamud, G., Handy, T.A., Prisbrey, S., Krauland, C.M., Klein, S.R., Harding, E.C., Wallace, R., Grosskopf, M. J., Marion, D.C., Kalantar, D., Giraldez, E., Drake, R.P., 2018. How high energy fluxes may affect Rayleigh–Taylor instability growth in young supernova remnants. Nat. Commun. 9 (1), 1564. https://doi.org/10.1038/s41467-018-03548-7.

Lei, W., Lu, X., Gong, W.M., 2023. Triggering interfacial instabilities during forced imbibition by adjusting the aspect ratio in depth-variable microfluidic porous media. Proc. Nat. Acad. Sci. 120 (50), e2310584120. https://doi.org/10.1073/pnas.2310584120.

Lenormand, R., Touboul, E., Zarcone, C., 1988. Numerical models and experiments on immiscible displacements in porous media. J. Fluid Mech. 189, 165–187. https://doi.org/10.1017/S0022112088000953.

Li, L., Kang, Y., Hu, Y., Pan, H., Huang, Y., Yuan, Q., 2025. Capillary number effects on two-phase flow and residual oil morphology in water and supercritical CO_2 displacement: A microfluidic study. Energy 316, 134503. https://doi.org/10.1016/j.energy.2025.134503.

Li, Y., Yang, Y., Sun, X., Yang, D., Zhang, N., Yang, H., Guo, H., Zheng, J., 2014. The application of laser confocal method in microscopic oil analysis. J. Petrol. Sci. Eng. 120, 52–60. https://doi.org/10.1016/j.petrol.2014.04.005.

Liu, C., You, Q., Wang, T., Zhou, B., Peng, W., Du, Y., Liu, Y., Li, Y., Dai, C., 2024. Study of microscopic imbibition and formation plugging mechanism of the compact oil reservoir based on SEM and NMR analysis. Fuel 357, 129672. https://doi.org/10.1016/j.fuel.2023.129672.

Lu, Y., Liu, D., Cai, Y., Li, Q., Zhou, Y., 2022. Spontaneous imbibition in coal with in-situ dynamic micro-CT imaging. J. Petrol. Sci. Eng. 208, 109296. https://doi.org/10.1016/j.petrol.2021.109296.

Lv, Q., Hou, J., Chen, J., Ji, Y., Cheng, Z., Lv, J., Zhong, J., 2025. Experimental study on elastic development characteristics and imbibition mechanism of shale oil reservoirs at micro-nano scale. Fuel 381, 133557. https://doi.org/10.1016/j.fuel.2024.133557.

Mahmoudzadeh, A., Fatemi, M., Masihi, M., 2022. Microfluidics experimental investigation of the mechanisms of enhanced oil recovery by low salinity water flooding in fractured porous media. Fuel 314, 123067. https://doi.org/10.1016/j.fuel.2021.123067.

Malenica, L., Zhang, Z., Angst, U., 2024. Towards improved understanding of spontaneous imbibition into dry porous media using pore-scale direct numerical simulations. Adv. Water Resour. 194, 104840. https://doi.org/10.1016/j.advwatres.2024.104840.

Niu, Z., Yang, Z., Chang, Y., Zhang, Y., Luo, Y., Chen, X., Zhao, X., 2022. Numerical studies on displacement-imbibition process of pore-network extracted from the microfluidic chip. J. Petrol. Sci. Eng. 215, 110686. https://doi.org/10.1016/j.petrol.2022.110686.

Odier, C., Levaché, B., Santanach-Carreras, E., Bartolo, D., 2017. Forced imbibition in porous media: A fourfold scenario. Phys. Rev. Lett. 119 (20), 208005. https://doi.org/10.1103/PhysRevLett.119.208005.

Park, S.Y., Ahn, T., Lee, H., Chen, Z., 2025. Application of Raman spectroscopy for analyzing the behavior of gases in sandstone reservoirs. Spectrochim. Acta Mol. Biomol. Spectrosc. 327, 125323. https://doi.org/10.1016/j.saa.2024.125323.

Saffman, P.G., Taylor, G., 1988. The penetration of a fluid into a porous medium or Hele-Shaw cell containing a more viscous liquid. Proc. Royal Soc. London Ser. A. Math. Phys. Sci. 245, 312–329. https://doi.org/10.1098/rspa.1958.0085.

Seetharaman, G.R., Devakumar, N.P., Deshmukh, M., Sangwai, J.S., 2025. Enhanced oil recovery by spontaneous imbibition of nanofluid assisted low saline alkali polymer in sandstone reservoir. J. Mol. Liq. 428, 127533. https://doi.org/10.1016/j.molliq.2025.127533.

Shoukry, A.E., Saraji, S., Piri, M., 2023. Two-phase displacement dynamics in fractured porous media of varying wettability states: A micromodel experimental investigation of matrix/fracture interactions. Adv. Water Resour. 176, 104447. https://doi.org/10.1016/j.advwatres.2023.104447.

Singh, D., Friis, H.A., Jettestuen, E., Helland, J.O., 2023. Pore-scale Ostwald ripening of gas bubbles in the presence of oil and water in porous media. J. Colloid Interface Sci. 647, 331–343. https://doi.org/10.1016/j.jcis.2023.05.070.

Southwick, J., Rijn, C.H., Pol, E., Batenburg, D.W.V., Azhan, A., Kalantar, A., Zulkifli, N., 2020. Advantages of an APS/AES seawater-based surfactant polymer formulation. SPE J. 25, 3494–3506. https://doi.org/10.2118/190296-pa.

Spildo, K., Sun, L., Djurhuus, K., Skauge, A., 2014. A strategy for low cost, effective surfactant injection. J. Petrol. Sci. Eng. 117, 8–14. https://doi.org/10.1016/j.petrol.2014.03.006.

Suetrong, N., Tosuai, T., Vo Thanh, H., Chantapakul, W., Tangparitkul, S., Promsuk, N., 2024. Predicting dynamic contact angle in immiscible fluid displacement: A machine learning approach for subsurface flow applications. Energy & Fuels 38 (5), 3635–3644. https://doi.org/10.1021/acs.energyfuels.3c04251.

Sukee, A., Nunta, T., Fongkham, N., Yoosook, H., Jeennakorn, M., Harbottle, D., Santha, N., Tangparitkul, S., 2022a. Effects of brine valency and concentration on oil displacement by spontaneous imbibition: an interplay between wettability alteration and reduction in the oil-brine interfacial tension. J. Mol. Liq. 365, 120089. https://doi.org/10.1016/j.molliq.2022.120089.

Sukee, A., Nunta, T., Haruna, M.A., Kalantariasl, A., Tangparitkul, S., 2022b. Influence of sequential changes in the crude oil-water interfacial tension on spontaneous imbibition in oil-wet sandstone. J. Petrol. Sci. Eng. 210, 110032. https://doi.org/10.1016/j.petrol.2021.110032.

Sun, Y., Xin, Y., Wei, L.N., Ding, F., Gao, Z., Liu, H., Tang, M., Du, X., Dai, C., 2022. Oil drop stretch and rupture behavior at throat and pore junction during imbibition with active nanofluid: A microfluidic approach. Colloids Surf. A Physicochem. Eng. Asp. 653, 130012. https://doi.org/10.1016/j.colsurfa.2022.130012.

Taman, A., Shoukry, A.E., Kubelka, J., Piri, M., 2025. Oil recovery enhancement by nanobubbles: Insights from high-pressure micromodel studies. J. Colloid Interface Sci. 693, 137647. https://doi.org/10.1016/j.jcis.2025.137647.

Tangparitkul, S., Sukee, A., Jiang, J., Tapanya, C., Fongkham, N., Yang, H., 2023. Role of interfacial tension on wettability-controlled fluid displacement in porous rock: A capillary-dominated flow and how to control it. Capillarity 9 (3), 55–64. https://doi.org/10.46690/capi.2023.12.02.

Tangparitkul, S., Akamine, T., Harbottle, D., Srisuriyachai, F., Yu, K., 2024. Discrepancy in oil displacement mechanisms at equivalent interfacial tensions: Differentiating contributions from surfactant and nanoparticles on interfacial activities. J. Mol. Liq. 414, 126304. https://doi.org/10.1016/j.molliq.2024.126304.

Tliba, L., Edokali, M., Moore, T., Choudhry, O., Glover, P.W.J., Menzel, R., Hassanpour, A., 2025. Spontaneous in-situ emulsification and enhanced oil recovery using functionalised silica nanoparticles: Insights from spontaneous imbibition and micromodel flooding tests. J. Mol. Liq. 424, 127021. https://doi.org/10.1016/j.molliq.2025.127021.

Wang, Y., Zhang, F., Liu, F., 2024. Thermo-hydro-mechanical (THM) coupled simulation of the land subsidence due to aquifer thermal energy storage (ATES) system in soft soils. J. Rock Mech. Geotech. Eng. 16 (6), 1952–1966. https://doi.org/10.1016/j.jrmge.2023.05.019.

Wu, D., Li, S., Zhang, N., Guo, Y., Liu, L., Wang, Z., 2023. A novel permeability model for hydrate-bearing sediments integrating pore morphology evolution based on modified Kozeny-Carman equation. Energy 277, 127723. https://doi.org/10.1016/j.energy.2023.127723.

Yadali Jamaloei, B., Asghari, K., Kharrat, R., Ahmadloo, F., 2010. Pore-scale two-phase filtration in imbibition process through porous media at high- and low-interfacial tension flow conditions. J. Petrol. Sci. Eng. 72 (3), 251–269. https://doi.org/10.1016/j.petrol.2010.03.026.

Yang, S., Kong, G., Cao, Z., Wu, Z., Li, H., 2022. Hydrodynamics of gas-liquid displacement in porous media: Fingering pattern evolution at the breakthrough moment and the stable state. Adv. Water Resour. 170, 104324. https://doi.org/10.1016/j.advwatres.2022.104324.

Yu, F., Gao, Z., Zhu, W., Wang, C., Liu, F., Xu, F., Jiang, H., Li, J., 2021. Experiments on imbibition mechanisms of fractured reservoirs by microfluidic chips. Petrol. Explor. Dev. 48 (5), 1162–1172. https://doi.org/10.1016/S1876-3804(21)60099-X.

Yu, W., Lo, J.H.Y., Adebayo, A.R., Rezk, M.G., Al-Yaseri, A., AlYousef, Z., 2025. Microfluidic study of CO_2 diffusive leakage through microfractures in saline aquifers for CO_2 sequestration. Adv. Water Resour. 200, 104960. https://doi.org/10.1016/j.advwatres.2025.104960.

Zhang, D., Campbell, J.M., Eriksen, J.A., Flekkøy, E.G., Måløy, K.J., MacMinn, C.W., Sandnes, B., 2023. Frictional fluid instabilities shaped by viscous forces. Nat. Commun. 14 (1), 3044. https://doi.org/10.1038/s41467-023-38648-6.

Zhang, J., Wang, D., 2022. Aqueous imbibition further investigation on contact area penetration enhancement for hydrocarbon extraction from tight rocks. J. Petrol. Sci. Eng. 208, 109206. https://doi.org/10.1016/j.petrol.2021.109206.

Zhang, S., Li, J., Coelho, R.C.V., Wu, K., Zhu, Q., Guo, S., Chen, Z., 2025. Lattice Boltzmann modeling of forced imbibition dynamics in dual-wetted porous media. Int. J. Multiphas. Flow 182, 105035. https://doi.org/10.1016/j.ijmultiphaseflow.2024.105035.

Zhong, Y., Li, Q., Gao, W., Wen, Y., Zhang, Y., 2025. A review of microfluidic technology for CO_2 sequestration in saline aquifers. J. Rock Mech. Geotech. Eng. https://doi.org/10.1016/j.jrmge.2025.01.018.